Lab on a Chip

RSC Publishing

PAPER

Dynamics of a microliquid prism actuated by electrowetting

Cite this: *Lab Chip*, 2013, **13**, 274

Duck-Gyu Lee,[a] Jaebum Park,[a] Jungmok Bae*[b] and Ho-Young Kim*[a]

Received 10th September 2012,
Accepted 19th October 2012

DOI: 10.1039/c2lc41024a

www.rsc.org/loc

A microliquid prism is a microchannel filled with two immiscible liquids, whose interface acts as a refractive surface. To steer a light beam that constructs optical images, the interface profile or the contact angle is modulated through electrowetting on a dielectric. Accurate, yet agile actuation of the liquid prism critically depends on the understanding of dynamics of the fluid interface. Here we fabricate liquid prisms, visualize the shape evolution of the interface, and theoretically model its dynamics. By comparing the magnitude of capillary forces to those of viscous, inertial and hydrostatic forces, we find that the meniscus motion within submillimetric channels is dominated by the capillary effect. The theoretical predictions for microscale meniscus dynamics are shown to agree well with the experimental measurements. We then discuss the formation of waves in millimetric liquid prisms, which may significantly limit fast and reliable operation of the optofluidic device.

I. Introduction

Electrowetting on dielectric (EWOD) is a technique to modify the contact angle of a conducting liquid on a dielectric surface by establishing an electrical potential difference between a dielectric-coated electrode and the liquid. This method to control fluid interfaces is free of physical fatigue and noise owing to the absence of mechanically moving parts and consumes relatively small power. Applications of EWOD include drop manipulation in microfluidics,[1,2] sample processing in biochips,[3,4] pigment transport in display devices,[5,6] and shape control of liquid lenses.[7,8] Here we investigate the application of EWOD to the development of microliquid prisms that steer light beams *via* motion of liquid interfaces acting as an optical refractive surface.[9,10] The applications of a microprism array include telescopic optics, laser radar,[11] solar lighting,[12] and three-dimensional displays.[13] In particular, three-dimensional displays based on a viewer tracking scheme, such as holography, are possible by distributing limited resources of the image panel adaptively to the viewers using microliquid prism arrays.

The use of EWOD to drive a liquid prism was first demonstrated by Smith *et al.*[9] with a long rectangular channel. Boer *et al.*[10] used a square pyramidal frustum for beam steering and demonstrated a feedback driving scheme for the accurate control of meniscus shapes and tilts. The previous studies focused on the equilibrium shapes of interfaces depending on the applied voltages, thus neither dynamic analysis nor measurement of liquid prisms in motion has been carried out so far. Although the dynamics of fluid interfaces under the effect of electrowetting have been actively studied for drops that spread, translate or split on solid surfaces,[14–17] the results cannot be directly applied to the dynamics of EWOD-driven liquid prism interfaces that involve motions of two immiscible liquids confined in narrow channels. Physical understanding of the liquid–liquid interface dynamics in the prism is essential for practical application of the device as an optical display – the dynamic response of the prism should be sufficiently fast and reliable to ensure a sharp transition between image frames. Therefore, here we fabricate liquid prisms, visualize the shape evolution of the interface, and theoretically model its dynamics. The theoretical framework constructed in this work can be useful for a variety of microfluidic or optofluidic devices, which either involve the motion of fluid–fluid interfaces or employ the electrowetting scheme to drive liquid flows.

II. Experimental

To fabricate a liquid prism that actuates a liquid–liquid interface by EWOD, we face two parallel silicon plates of 30 mm in width separated by a gap $d \in [0.3\text{–}2]$ mm, as shown in Fig. 1. The plates are coated with molybdenum (electrode) and dielectric layers of silicon nitride and parylene C. The gaps are sealed by transparent polytetrafluoroethylene (PTFE)-coated glass plates with epoxy. The cell is loaded with a mixture of 1% dodecane and 99% 1-chloronaphthalene (referred to as liquid L) and then 0.85 wt% aqueous solution of polyacrylic acid

---

[a] *School of Mechanical and Aerospace Engineering, Seoul National University, Seoul 151-744, Korea. E-mail: hyk@snu.ac.kr*

[b] *Samsung Advanced Institute of Technology, Samsung Electronics Co., Ltd., Yongin, Gyeonggi-Do 446-712, Korea. E-mail: jungmok.bae@samsung.com*

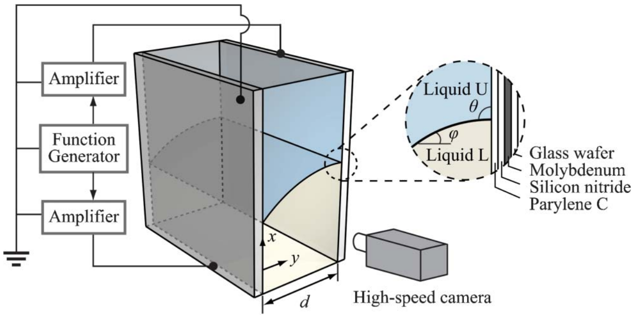

Fig. 1 Schematic of a liquid prism and its liquid–liquid interface actuated by electrowetting on a dielectric.

(referred to as liquid U), whose interface is known to exhibit a high refractive index over 1.6 and robust electrowetting performance.[18] The density, ρ, and viscosity, μ, of the liquids and the interfacial tension between the two liquids, γ, are listed in Table 1. By applying voltages at the individual electrodes, the contact angle at the two faces can be separately controlled. The electrodes on each side are connected to high voltage amplifiers (AA Lab Systems A-301 HS) that amplify the driving voltage generated by a function generator (National Instruments NI9263). The function generator signals ac (alternating current) voltage in square waves of 1.5 kHz in frequency to prevent damage of the dielectric surface by charge accumulation, which frequently occurs when dc (direct current) is used.[12,19] The function generator is controlled by a personal computer *via* a Labview (National Instruments) interface. The liquids are electrically grounded. Upon applying voltage, the motion of the liquid prism is observed through the transparent side of the cell *via* a high-speed video camera (Photron APX-RS) recording images upto 1500 frames per second. Then the digital images are analyzed to determine the position of contact lines and contact angles at the two faces. Because the electrode plates are much longer in their sides than the gap, the interface motion can be considered two-dimensional.

Fig. 2 shows the image sequences of the liquid–liquid interfaces for different sizes of gap (0.32, 0.95 and 1.93 mm). Initially, the equilibrium contact angle measured through liquid U (see Fig. 1 for the definition of the contact angle θ) is maintained greater at the left wall than at the right, so that the interface is slanted to the right. Here the equilibrium angle corresponds to the static contact angle of the liquid–liquid interface determined by an applied voltage. Fig. 3 shows the experimental measurement results of the equilibrium contact angle that decreases with voltage. To reverse the inclination, the voltage at the left wall (V_l) is suddenly raised to decrease the equilibrium contact angle at the left wall ($\theta_{\mathrm{l},0}$). At the same time, the voltage at the right wall (V_r) is suddenly reduced to increase the equilibrium contact angle at the right wall ($\theta_{\mathrm{r},0}$). Although the voltage at the walls is adjusted instantaneously, it takes a finite time for the liquid interface to move to an equilibrium position corresponding to the newly applied voltage condition. To quantitatively understand such dynamic behavior of the interface, we develop a hydrodynamic model that predicts the shape of the meniscus with time in the following.

Table 1 Physical properties of the liquids

Liquid	ρ (kg m^{-3})	μ (kg m^{-1} s^{-1})	γ (mN m^{-1})
U	1143	0.0013	7.64
L	1179	0.0027	

III. Theoretical formulation

The equation describing the shape of a deforming meniscus is given by the balance of normal stresses at the boundary between two liquids:[20]

$$p_\mathrm{U} - p_\mathrm{L} - \gamma\kappa = 2[(\mu e_{ij} n_i n_j)_\mathrm{U} - (\mu e_{ij} n_i n_j)_\mathrm{L}] \qquad (1)$$

where p is the pressure, subscripts U and L denote the upper and lower liquids, respectively, e_{ij} is the strain rate tensor, $e_{ij} = \frac{1}{2}\left(\partial u_i/\partial x_j + \partial u_j/\partial x_i\right)$ with u being the velocity, and n is the unit normal vector. The curvature κ is given by $\kappa = -\cos\varphi(\mathrm{d}\varphi/\mathrm{d}y)$ in a two-dimensional space with φ being the slope of the meniscus to the horizontal. In principle, integrating κ in eqn (1) with known pressure distribution and velocity fields yields the meniscus profile. However, here we show that eqn (1) can be greatly simplified for viscous liquids confined in a small channel. We begin with comparing the viscous shear stress (τ_v, the right-hand side of eqn (1)) and the capillary pressure ($\tau_c = \gamma\kappa \sim \gamma/d$), where $\sim$ signifies "is scaled as". Writing the characteristic velocity of the interface as U, the ratio of the viscous stress to the capillary pressure is scaled as $\tau_v/\tau_c \sim (\mu U/d)/(\gamma/d) \sim \mu U/\gamma$, where μ is for the more viscous liquid. The dimensionless ratio is referred to as the capillary number, $Ca = \mu U/\gamma$. Because $U \in [0.01\text{–}0.06]$ m s^{-1} based on the speed of the contact line and $\mu = 0.0027$ kg m^{-1} s^{-1} in our experiments, the order of Ca ranges between 10^{-3} and 10^{-2}, indicating that viscous forces are negligibly small compared to the capillary force. The inertial effects can be evaluated by comparing the dynamic pressure, τ_p, scaled as $\tau_p \sim \rho U^2$ with τ_c, where ρ is the density of the denser liquid. The ratio τ_d/τ_c corresponds to the Weber number, $We = \rho U^2 d/\gamma$. In our experiments, We decreases from approximately 0.92 to 0.018 as the gap decreases from 1.93 mm to 0.32 mm, indicating that the inertial effects vanish as the gap decreases to submillimetric scales. Finally, we consider a ratio of the hydrostatic pressure, $\tau_h \sim (\rho_L - \rho_U)gh$, with h being the channel height, to τ_c, which corresponds to the Bond number: $Bo = (\rho_L - \rho_U)ghd/\gamma$. Since Bo is of the order of 10^{-3} in our experiments, the hydrostatic effects can also be neglected as compared to the capillary effect. These simplifications imply that the pressure is uniform inside each liquid without being perturbed by fluid motions, whose viscous and dynamic effects are too weak compared to that of capillarity in submillimetric channels. Then eqn (1) reduces to $\kappa = C$, where C is a function that depends only on time. The liquid prism in a microcell moves in a

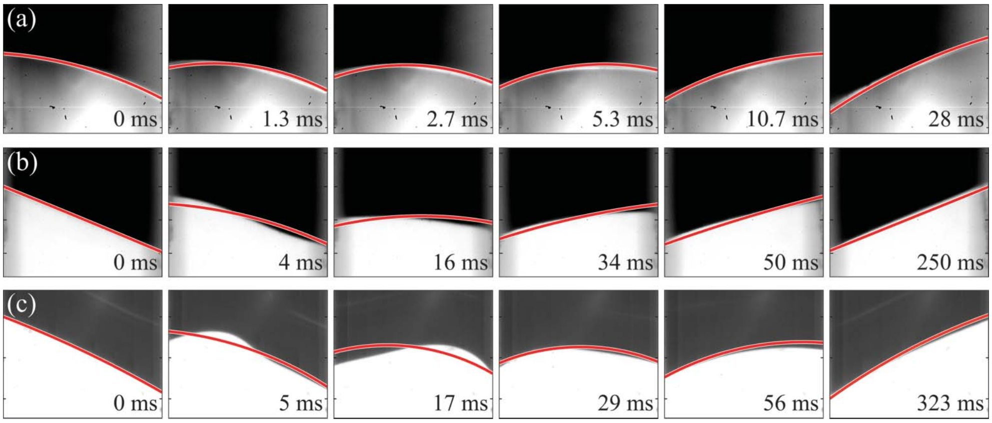

Fig. 2 Time series of the interface motion between liquids U and L in a channel with a gap (a) $d = 0.32$ mm, (b) $d = 0.95$ mm, (c) $d = 1.93$ mm. The red line corresponds to the theoretical prediction.

quasi-static manner as the contact line is driven by the voltage change with its meniscus always being a segment of a circle.

Now the equation of meniscus shape is written as

$$\begin{aligned}\frac{\mathrm{d}y}{\mathrm{d}\varphi} &= -\frac{\cos\varphi}{C}\\ \frac{\mathrm{d}x}{\mathrm{d}\varphi} &= -\frac{\sin\varphi}{C}\end{aligned} \tag{2}$$

To determine C and two constants resulting from integration of eqn (2), we use the mass conservation relation and the following boundary conditions:

$$\begin{aligned}x &= x_\mathrm{l} \ \text{ at } \ \mathrm{y} = 0\\ x &= x_\mathrm{r} \ \text{ at } \ \mathrm{y} = d\end{aligned} \tag{3}$$

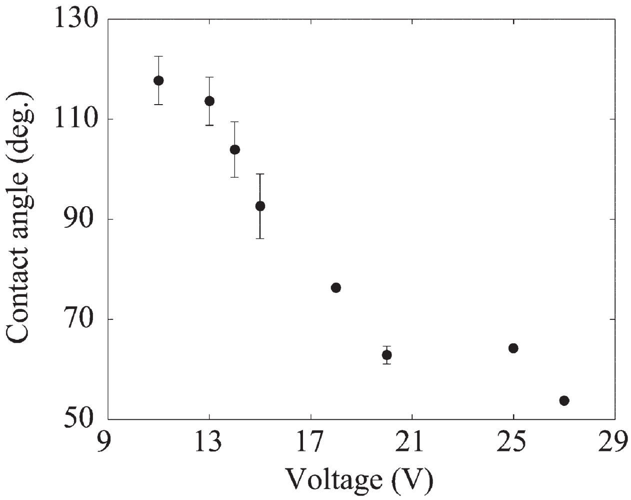

Fig. 3 Equilibrium contact angle *versus* voltage applied between the liquids (0.2 wt% polyacrylic acid aqueous solution and a mixture of 1% dodecane and 99% 1-chloronaphthalene) and the electrode beneath the dielectric film of silicon nitride and parylene C.

where x_l and x_r denote the position of left and right contact lines, respectively. To close the mathematical formulation which predicts the shape evolution of the meniscus with time, we need a relationship between the contact line velocity, U_c, and the dynamic contact angle. While a number of models have been suggested to relate the contact line velocity and the dynamic contact angle in the absence of electrical effects,[21–24] the understanding of contact line velocities driven by electrowetting is still far from complete.[25,26] Nonetheless, it is well known that U_c increases as the difference between the dynamic and equilibrium contact angles grows whether electrically driven or not. Hence, we adopt the following form:

$$U_c = \frac{1}{\xi}\gamma(\cos\theta_0 - \cos\theta_d) \tag{4}$$

where ξ corresponds to the contact line friction coefficient, θ_0 is the equilibrium contact angle depending on the voltage and θ_d is the instantaneous dynamic contact angle. This relationship is consistent with a model based on the molecular kinetic theory,[23,24,27] where $\xi \sim T/(f\lambda^3)$, with T being the temperature and f and λ the typical characteristic frequency and length of molecular displacements, respectively. The effects of liquid viscosities on ξ would be non-negligible especially when one liquid displaces the other as in our experiments. We measured contact line velocities as a function of $\gamma(\cos\theta_0 - \cos\theta_d)$ as shown in Fig. 4 to empirically determine ξ. We find that $\xi = -2.02$ kg m^{-1} s^{-1} when liquid L displaces liquid U (positive velocity) and $\xi = -5.64$ kg m^{-1} s^{-1} when liquid U displaces liquid L (negative velocity).

To numerically calculate the shape evolution of the meniscus, we begin with obtaining the initial shape of the meniscus, which corresponds to the initial positions (x_l and x_r) and slopes ($\theta_{\mathrm{l},0}$ and $\theta_{\mathrm{r},0}$), by integrating eqn (2) from $y = 0$ to d. Now the voltages at the left and right walls are suddenly changed, thus the original contact angles (the equilibrium contact angles in the previous voltage condition) are different from the new equilibrium values. Such a contact angle

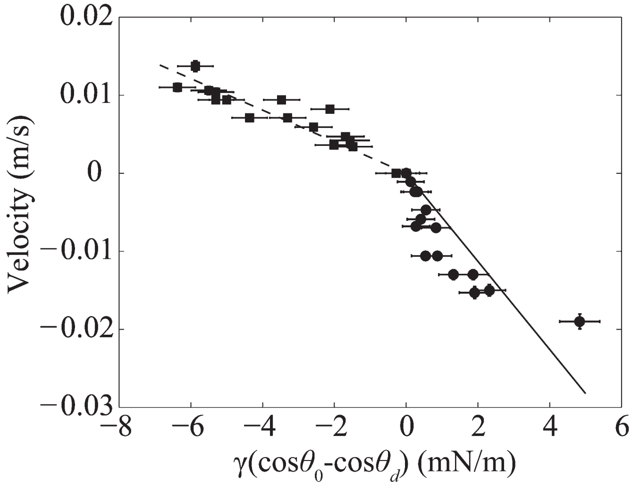

Fig. 4 Contact line velocity *versus* $\gamma(\cos\theta_0 - \cos\theta_d)$. The positive velocity (squares and dashed line) corresponds to liquid L displacing liquid U and the negative velocity (circles and solid line) to liquid U displacing liquid L. The slope of the best-fitting straight line corresponds to $1/\xi$. The experiments were performed in a channel of 0.32 mm in gap width, where the capillary effects dominate the interface motion.

difference gives rise to contact line velocity as described by eqn (4). With new positions of the contact lines after a small time step, we integrate eqn (2) to iteratively find new contact angles and C that conserve volumes of upper and lower liquids. The contact line velocities are now renewed according to the new contact angles, which are used to find the contact line positions in the next time step. We repeat this process until the dynamic contact angles match the equilibrium contact angles corresponding to the voltage conditions, when the meniscus evolution ends.

IV. Results and discussion

To verify our theory, we compare the theoretical predictions of temporal evolution of the meniscus shape and contact line position with the experimental results as shown in Fig. 2 and 5. Fig. 5 shows that the contact line movement is rapid in the early stages when the difference between the equilibrium and dynamic contact angles is large while it slows down as the dynamic angle approaches the equilibrium value. In submillimetric channels of 0.32 mm in gap width, Fig. 5(a), the theoretically predicted contact line positions are in good agreement with the experimental measurements. The excellent agreement between theory and experiment is also found for meniscus shapes, Fig. 2(a), where the experimentally observed meniscus indeed assumes the shape of a circular arc. These results reveal that our hydrodynamic analysis neglecting viscous, inertial and hydrostatic effects as compared to those of capillarity is fairly accurate for submillimetric channels.

As the channel width increases to 0.95 and 1.93 mm, a non-negligible discrepancy between the theoretical contact line positions and the experimental results is observed in Fig. 5(b) and (c) although the overall tendency is still well predicted. The discrepancy is mainly attributed to the interfacial waves generated in the early stages as can be clearly seen in Fig. 2(c). The waves are due to inertial effects which have been neglected in our model.

To rigorously analyse the onset conditions for interfacial waves between two viscous liquids bound by vertical walls is beyond the scope of this work. However, here we present a simple analysis to understand the mechanism and conditions of the wave generation. The motion of the refractive surface, or the tilting of the meniscus, in the liquid prism is driven by the sudden change of the voltages at the wall electrodes. If the consequent contact line speed is so fast that the entire meniscus cannot instantaneously respond to the motion of its edge, the meniscus deformation appears to propagate from one edge to the channel centre. In Fig. 2(c), the contact line speed on the left wall is greater than that on the right wall because of a smaller ξ (corresponding to liquid U displacing liquid L), thus the motion of the left contact line dominates the wave behaviour. As shown in Fig. 6, which plots the distance of the wave crest from the left wall *versus* time, the wave generated at the left edge propagates to the right (time

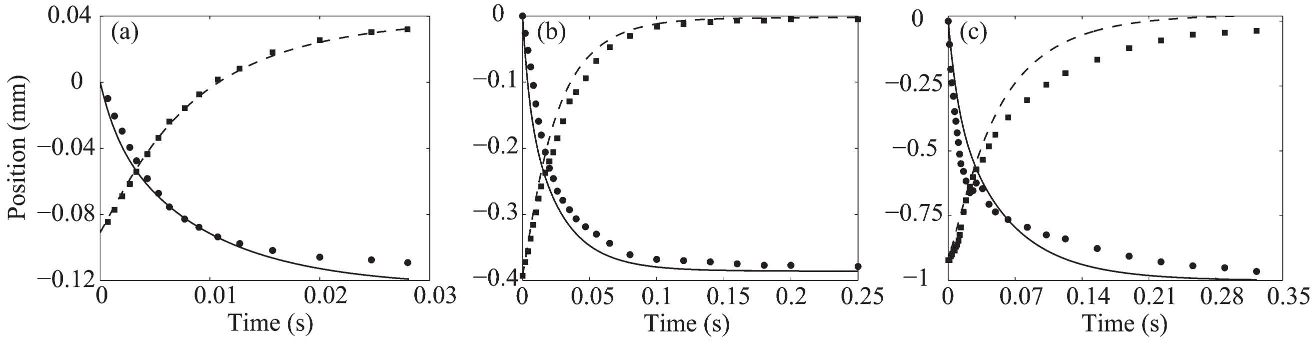

Fig. 5 Comparison between theoretical predictions and experimental results of temporal evolution of contact line position, whose images are shown in Fig. 2. The circles and squares are the experimental results for the contact lines at the left and right walls, respectively. The solid and dashed lines correspond to the theoretical predictions for the contact lines at the left and right walls, respectively. The coordinates are chosen such that the contact line at the left wall starts at $x = 0$. (a) $d = 0.32$ mm, (b) $d = 0.95$ mm, (c) $d = 1.93$ mm.

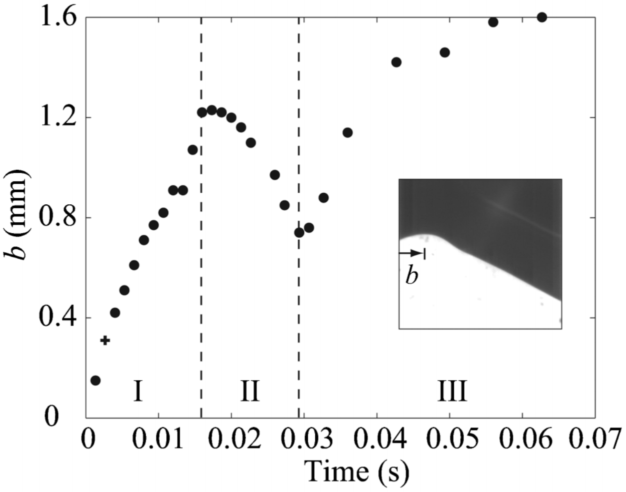

Fig. 6 Horizontal distance of wave crest from the left wall, *b*, *versus* time for the wave shown in Fig. 2(c). The inset shows the wave propagating to the right corresponding to the cross in time range I.

range I), moves back to the left upon hitting the right wall (time range II), and reflects back to the right (time range III). The phase speed of the wave in time range I is measured to be 77.3 mm s^{-1}. We note that the minimum phase velocity of interfacial waves of two different fluids superposed one over the other, *c*, is given by[28]

$$c^2 = 2gl_c \frac{\rho_L - \rho_U}{\rho_L + \rho_U} \tag{5}$$

where *g* is the gravitational acceleration and l_c is the capillary length defined as $l_c = \sqrt{\gamma/(\Delta\rho g)}$ with $\Delta\rho = \rho_L - \rho_U$. Hydrodynamic theory dictates that interfacial waves occur only when the phase velocity is greater than *c*. Although this theory is strictly valid for potential flows without bounds, we compare *c* with the experimentally measured phase velocity. The minimum phase velocity, *c*, corresponding to our experimental conditions is calculated to be c = 37.6 mm s^{-1}, which is smaller than the experimentally measured phase velocity, 77.3 mm s^{-1}, as theoretically predicted.

For the interfacial wave to emerge and subsequently propagate, the following two conditions must be fulfilled. First, the dynamic pressure, τ_d, must overcome the capillary pressure, τ_c, in order to change the curvature of the interface. It is the Weber number, *We*, that measures the relative magnitude of τ_d to τ_c. Our experimental results indicate that the wave is absent for $We < 0.018$ (corresponding to the characteristic contact line velocity U_c = 19 mm s^{-1}, Fig. 2(a)) while a very weak wave appears for $We > 0.020$ (corresponding to U_c = 12 mm s^{-1}, Fig. 2(b)). Thus the threshold *We* for wave generation is found to be located around 0.019. For the strong wave as shown in Fig. 2(c), *We* is found to be 0.92 for U_c = 55 mm s^{-1}. Second, the interfacial motion must be so fast that the viscous effect cannot dampen the entire flow field. The time scale for the viscous diffusion to occur across the contact line movement distance, $d\tan\alpha$, is estimated as $t_v \sim (d\tan\alpha)^2/\nu$, where α is the angle that the meniscus should tilt and ν the kinematic viscosity of the thicker liquid. Whereas, the time scale for meniscus tilting is given by $t_m \sim d\tan\alpha/U$. The ratio of t_v to t_m corresponds to the Reynolds number, defined as $Re = Ud\tan\alpha/\nu$. The wave is observed to occur for $Re > 2.1$ (Fig. 2(b)) and absent for $Re < 0.9$ (Fig. 2(a)), thus the threshold *Re* is located between 0.9 and 2.1. For Fig. 2(c), where the strong wave is generated, $Re = 22$. For reliable operation of liquid prisms, one needs to make sure that its dimensions and operation speeds avoid the conditions that generate waves, given in terms of *We* and *Re*.

V. Conclusions

To investigate the dynamics of a microliquid prism actuated by electrowetting, we developed a hydrodynamic model, which enables us to predict the temporal evolution of the meniscus shape. By comparing the magnitude of capillary forces to those of dynamic, viscous and hydrostatic forces, we found that the meniscus motion within submillimetric channels is dominated by the capillary effect, thus its shape can be modeled as a circular arc. The theoretical predictions were shown to be in good agreement with the measurement results of the experiments using a microscale liquid prism. We observed interfacial waves in millimetric liquid prisms, which were found to occur for high Weber and Reynolds numbers. Although the millimetric pixels are less realistic in practical devices with a high display resolution, they allow us to cover a wide range of nondimensional parameter space.

Our theoretical and experimental study allows us to scale the settling time, t_s, or the time taken for a meniscus to reach a new equilibrium, as $t_s \sim \xi d/(\gamma\cos\alpha)$, where we have substituted $U \sim (\gamma/\xi)\sin\alpha$ in t_m of the previous section. This implies that to reduce the settling time, or to increase the switching rate, one needs to choose a combination of liquids with a high interfacial tension (γ) and a dielectric coating with a low contact line friction coefficient (ξ) as well as reducing the cell size (d). Here we note that increasing the actuation frequency, or switching rate, even within submillimetric prisms may cause the corresponding *We* and *Re* to exceed their threshold values for wave suppression. Our study of interfacial waves in millimetric pixels can guide us in designing devices, selecting materials and operating actuation circuitry in such a way that waves in high-speed microscale liquid prisms can be avoided.

Many questions still remain to be explored to further our understanding and control of liquid prism dynamics. On the basis of our two-dimensional study, the dynamics of interfaces within three-dimensional liquid cells need to be understood, which will require numerical simulations and more sophisticated visualization techniques. The onset conditions of interfacial waves would be also modified as the three-dimensional effects come into play. Finally, the interference of electric fields which may occur as the gap between the electrodes is reduced with device miniaturisation should be considered in the future. Understanding the dynamics of liquid–liquid interfaces as bound by microscale chambers can benefit the development of a variety of optofluidic devices such as lenses, mirrors and waveguides in addition to prisms.[29]

Acknowledgements

This work was supported by Samsung Electronics and National Research Foundation (Grant Nos. 2011-0030744 and 2012-008023) of Korea, and administered *via* SNU-IAMD.

References

1 S. K. Cho, H. Moon and C.-J. Kim, *J. Microelectromech. Syst.*, 2003, **12**, 70–80.
2 V. K. Pamula, P. Paik, J. Venkatraman, M. G. Pollack and R. B. Fair, *Proc. IEEE MEMS*, 2001, 8–10.
3 V. Srinivasan, V. K. Pamula and R. B. Fair, *Lab Chip*, 2004, **4**, 310–315.
4 R. Sista, Z. Hua, P. Thwar, A. Sudarsan, V. Srinivasan, A. Eckhardt, M. Pollack and V. Pamula, *Lab Chip*, 2008, **8**, 2091–2104.
5 R. A. Hayes and B. J. Feenstra, *Nature*, 2003, **425**, 383–385.
6 J. Heikenfeld and A. J. Steckl, *Appl. Phys. Lett.*, 2005, **86**, 151121.
7 B. Berge and J. Peseux, *Eur. Phys. J. E: Soft Matter Biol. Phys.*, 2000, **3**, 159–163.
8 S. Kuiper and B. H. W. Hendriks, *Appl. Phys. Lett.*, 2004, **85**, 1128–1130.
9 N. R. Smith, D. C. Abeysinghe, J. W. Haus and J. Heikenfeld, *Opt. Express*, 2006, **14**, 6557–6563.
10 B. de Boer, F. Suijver, M. Megens, S. Deladi and S. Kuiper, *J. Appl. Phys.*, 2010, **107**, 063101.
11 P. F. McManamon, P. J. Bos, M. J. Escuti, J. Heikenfeld, S. Serati, H. Xie and E. A. Watson, *Proc. IEEE*, 2009, **97**, 1078–1096.
12 J. Cheng and C.-L. Chen, *Appl. Phys. Lett.*, 2011, **99**, 191108.
13 Y. Takai, R. Koshiishi, S. Kirita, M. Tsuchiya, Y. Watanabe, K. Takahashi, Y. Imai and Y. Shimpuku, in *Proc. IEEE MEMS*, 2012, 632–635.
14 C. Decamps and J. De Coninck, *Langmuir*, 2000, **16**, 10150–10153.
15 H. Ren, R. B. Fair, M. G. Pollack and E. J. Shaughnessy, *Sens. Actuators, B*, 2002, **87**, 201–206.
16 H.-W. Lu, K. Glasner, A. L. Bertozzi and C.-J. Kim, *J. Fluid Mech.*, 2007, **590**, 411–435.
17 J. M. Oh, S. H. Ko and K. H. Kang, *Phys. Fluids*, 2010, **22**, 032002.
18 J. Zhang, D. Van Meter, L. Hou, N. Smith, J. Yang, A. Stalcup, R. Laughlin and J. Heikenfeld, *Langmuir*, 2009, **25**, 10413–10416.
19 M. Dhindsa, S. Kuiper and J. Heikenfeld, *Thin Solid Films*, 2011, **519**, 3346–3351.
20 G. K. Batchelor, *An Introduction to Fluid Dynamics*, 1967, Cambridge Univ. Press, Cambridge, UK.
21 R. L. Hoffman, *J. Colloid Interface Sci.*, 1975, **50**, 228–241.
22 P.-G. de Gennes, *Colloid Polym. Sci.*, 1986, **264**, 463–465.
23 T. D. Blake and J. M. Haynes, *J. Colloid Interface Sci.*, 1969, **30**, 421–423.
24 T. D. Blake, *J. Colloid Interface Sci.*, 2006, **299**, 1–13.
25 L. Y. Yeo and H.-C. Chang, *Phys. Rev. E: Stat., Nonlinear, Soft Matter Phys.*, 2006, **73**, 011605.
26 M. Schneemilch, W. J. J. Welters, R. A. Hayes and J. Ralston, *Langmuir*, 2000, **16**, 2924–2927.
27 T. D. Blake, A. Clarke and E. H. Stattersfield, *Langmuir*, 2000, **16**, 2928–2935.
28 L. M. Milne-Thomson, *Theoretical Hydrodynamics*, 5th edn, 2011, New York, Dover.
29 L. Pang, H. M. Chen, L. M. Freeman and Y. Fainman, *Lab Chip*, 2012, **12**, 3543–3551.